PNAS
www.pnas.org

Supplementary Information for

Evidence of a Liquid-Liquid Transition in a Glass-forming Ionic Liquid

Matthew A. Harris, Thomas Kinsey, Durgesh V. Wagle, Gary A. Baker, Joshua Sangoro

Joshua Sangoro.
E-mail: jsangoro@utk.edu

This PDF file includes:

Supporting Information Text

Materials and Methods

Synthesis of $[P_{666,14}]^+[BH_4]^-$

The ionic liquid used in this study was synthesized from $[P_{666,14}]^+[Cl]^-$ by metathesis methods.(1–5) Sodium borohydride (213462, 99%), chloroform (CX1059-1), and sodium hydroxide (795429, ≥97%) were acquired from MilliporeSigma (St. Louis, MO). The salt $[P_{666,14}]^+[Cl]^-$ (>93%, CYPHOS® IL 101; CAS No. 258864-54-9) was a product of Cytec Canada Inc. (Cytec is currently owned by Solvay, Houston, TX).

To initiate ionic liquid synthesis, 10.0g (19.3mmol) of $[P_{666,14}]^+[Cl]^-$ was introduced to a 250mL round bottom flask already containing 100mL of chloroform, followed by stirring for 30 minutes. To this reaction mixture, 1.0 equivalent of the sodium salt ($NaBH_4$) was added, followed by the addition of 100mL of Millipore water (18.2MΩcm). The reaction mixture was stirred for 2 hours, then allowed to stand for an additional 30 minutes for chloroform-water phase separation. Centrifugation was performed to encourage phase disentanglement. The dense chloroform layer was washed with Millipore water five times to remove traces of NaCl by-product residing within the organic layer. Following aqueous washes, the chloroform layer was taken and dried over anhydrous $MgSO_4$. The chloroform layer was filtered through sintered glass to remove the drying agent and the chloroform was removed on a rotary evaporator to isolate the ionic liquid as a free-flowing liquid.

^{1}H NMR (500MHz, $CDCl_3$) spectra of $[P_{666,14}]^+[BH_4]^-$, assigned as follows, validate a successful synthesis.

$[P_{666,14}]^+[BH_4]^-$: δ 2.363 (m, 8H), 1.718 (s, 2H), 1.520 (m, 16 H), 1.325 (m, 14 H), 1.267 (m, 16H), 0.909 (t, 12H), 0.268 (s, 1H), 0.105 (s, 1H), –0.058 (s, 1H), –0.222 (s, 1H)

Wide-angle X-ray Scattering

The wide-angle X-ray scattering (WAXS) measurements were performed on the Xenocs Xeuss 3.0 SAXS instrument at the Joint Institute for Advanced Materials. The sample was first dried under vacuum ($< 10^{-6}$ bar) at 340K for 24 hours and then loaded into a fused silica capillary tube with 1.5mm outside diameter and 0.01mm wall thickness. The capillary tube was sealed with a clear epoxy prior the measurement. The temperature of the sample was controlled with a Linkam HFSX350 stage to within ±0.1K using liquid nitrogen as a coolant. The scattering intensity was measured under vacuum in the q-range from 0.13 to 3.9 $Å^{-1}$. The sample was initially measured at room temperature and then cooled to 195K (below T_g) at 10K/min. The sample was held at each temperature for 60s before collecting data over a 120s integration time. Measurements were taken at a series of temperatures upon heating the sample from below T_g back to room temperature.

Raman Spectroscopy

Raman measurements were performed using the Horiba LabRAM HR Evolution confocal Raman microscope with a 532nm excitation laser at 50% power, a 50x LWD objective, over three 15s accumulations, and 1800 gratings per mm filter to achieve 0.5cm^{-1} resolution. The sample was first dried under vacuum ($< 10^{-6}$ bar) at 340K for 24 hours. A drop of the sample was then loaded into a Linkam THMS600 temperature stage with silica windows to control the temperature to within ±0.1K using liquid nitrogen as the coolant, and the sample thickness was maintained at approximately 150μm using Teflon spacers. The sample was measured in the temperature range from 183K to 253K on cooling at 5K/min and heating at 10K/min pausing at each temperature for the duration of the measurement. Variations between the cooling and heating data were minimal.

Broadband Dielectric Spectroscopy

Broadband dielectric spectroscopy (BDS) measurements were performed in the frequency range of 10^{-1}-10^7Hz using a Novocontrol High Resolution Dielectric Alpha Analyzer with a Quatro liquid nitrogen temperature control system with ±0.1K temperature stability. The BDS measurements were carried out using gold-plated brass electrodes, 20mm in diameter, with Teflon spacers approximately 150μm in thickness. The sample was dried under vacuum ($< 10^{-6}$ bar) at 340K for 24 hours prior to being loaded between the electrodes using a syringe and inserted into the cryostat. Prior to measurement, the samples were annealed at 340K for more than 2 hours to ensure the spectra were not changing with time. Dielectric spectra were collected in 5K intervals on cooling from 340K to 150K and then on heating back to 340K in 10K intervals. This temperature sweep was repeated to ensure thermal reproducibility. For each temperature point, the sample took approximately 10 minutes for the temperature to stabilize and 5 minutes to measure the full frequency range. For temporal dielectric measurements the sample was prepared as described above. The sample was initially heated to 340K to equilibrate the high-temperature liquid structure. The sample was then rapidly cooled at about 10K/min to 210K in between T_g and T_{LL}. Once the temperature stabilized measurements were performed from 10^{-1}-10^7Hz every 360s up to 1hr.

Differential Scanning Calorimetry

Differential scanning calorimetry (DSC) measurements were conducted using a TA Instruments Q2000 DSC instrument. The sample was weighed into an aluminum pan of predetermined weight using a Mettler Toledo microbalance with an accuracy of

0.1μg and hermetically sealed before being loaded into the DCS instrument. An empty aluminum pan of the same type was used as a reference. The sample was initially heated to 340K to erase its thermal history. The DSC data was measured at a temperature ramp rate of 10K/min from 340K down to 150K and back up to 340K. This temperature sweep was cycled 3 times to ensure thermal reproducibility of the data.

Supplementary Text

Analysis of WAXS data

The WAXS data was processed in an iterative fashion by first fitting the raw intensity ($I(q)$) data at 300K (Fig. S1) using two Teubner-Strey functions(6), given by Eqn. S1, to describe the $q < 1\text{Å}^{-1}$ range combined with three Lorentzian functions (Eqn. S2) to account for the $q > 1\text{Å}^{-1}$ range.

$$S_{TS}(q) = 4\pi \frac{\Delta^2 cos\varphi - (q^2 - q_0^2) sin\varphi}{\Delta^4 + (q^2 - q_0^2)^2} \quad [1]$$

$$S_L(q) = I_0 \frac{\gamma^2}{\gamma^2 + (q - q_0)^2} \quad [2]$$

The data from the fit was then normalized to give intensity values of order unity. After that, the pair-distribution function (PDF), $g(r)$, was calculated from the normalized fit data according to Eqn. S3.(7)

$$g(r) = 1 + \frac{1}{2\pi^2 r \rho_0} \int_0^\infty q[S(q) - 1] sin(qr) dq \quad [3]$$

The normalization of the $I(q)$ was then adjusted so that the limit of $g(r)$ as $r \to \infty$ approaches a value of 1. Once this criteria was achieved for the $I(q)$ at 300K, yielding a normalization factor of 163, the same factor was applied to the $I(q)$ for the other temperatures to obtain the structure factor, $S(q)$. Density values necessary for the calculation of $g(r)$ were assumed to be linear as a function of temperature and were estimated based on correlations found in the literature.(8)

The $S(q)$ data at each temperature were fit using the same set of functions described above and the fit data were used to calculate $g(r)$. From the fitting parameters in the Teubner-Strey function the periodicity, d, and the correlation length, ξ, can be extracted from the relations in Eqn. S4 and S5.(6)

$$\Delta^2 = \frac{4\pi}{\xi d} \quad [4]$$

$$q_0^2 = \left(\frac{2\pi}{d}\right)^2 - \frac{1}{\xi^2} \quad [5]$$

These relations were used to determine d and ξ of the polarity alternation structure (Fig. 1C and 1D in the main text) and the charge alternation structure (Fig. S2A and S2B). Note that the periodicity of the charge alternation structure (d_{ch}, Fig. S2A) is independent of temperature while the correlation length (ξ_{ch}, Fig. S2B) shows a discontinuity at T_{LL}. This indicates that the interionic distances, reflected by d_{ch}, are governed primarily by Coulombic interactions and steric effects while ξ_{ch} is sensitive to the morphology of the liquid. The increase in ξ_{ch} below T_{LL} reflects the change from a single-stranded morphology to a double-stranded one. The peak positions from the Lorentzian fits, q_0, can be converted to real-space lengths using $d = 2\pi/q_0$. This is specifically pertinent to analyzing the temperature dependence of the charge adjacency peak around 1.8Å^{-1} shown in Fig. S2C. The length scale of the charge adjacency correlation are taken as a proxy of density correlations since this correlation reflects the average distance from a reference ion to its nearest neighbor counterion. The length scale, d_{adj}, contracts almost monotonically as the temperature of the $[P_{666,14}]^+[BH_4]^-$ IL is decreased from 300K to $T_g \approx$198K. Similarly, the inverse cube of d_{adj} increases almost monotonically across the same temperature range (Fig. S2D) indicating an increase in the overall density of the IL. A slight kink in these quantities is observed around the T_{LL} reflecting a slight decrease in density at the LLT. These effects are small but they may indicate that the density of the system is affected by the structural reorganization accompanying the liquid-liquid transition. This is unexpected since the density correlation is largely governed by the competition between steric effects due to the long cationic alkyl chains and electrostatic attraction between the cation and anion, both of which are not significantly altered by the specific morphology of the liquid, but primarily influenced by the energetics of the system.

An important quantity in understanding the structural reorganization at the LLT is the average coordination number, n_{av} (Fig. 1E in the main text). This can be calculated from $g(r)$ using Eqn. S6.(7)

$$n_{av} = 4\pi\rho_0 \int_{r_1}^{r_2} g(r) r^2 dr \quad [6]$$

By taking r_1 and r_2 as the first and second minima in $g(r)$, this equation can be used to calculate the coordination number of the IL in the first shell corresponding to nearest neighbor ions. The quantity of n_{av} can be regarded as a proxy for the bond order parameter from the two-order parameter model of Tanaka.(9) Changes to this parameter within the temperature range from the high temperature liquid down to the glass transition temperature are indications of an increase in the number of locally-favored structures leading to the first order liquid-liquid transition observed in $[P_{666,14}]^+[BH_4]^-$.

Analysis of Raman spectra

Particular regimes of the Raman spectra identified as reflective of the configuration of alkyl chains(10) were fit using a series of Gaussian peaks in order to quantify peak positions, intensities, and widths. Regions of interest included the $\nu(C-C)$ region between 1065 and 1130cm^{-1}, the $\tau(CH_2)$ region around 1300cm^{-1}, the $\delta(CH_2)$ and $\delta_a(CH_3)$ region between 1440 and 1458cm^{-1}, and the $\nu(CH_{2/3})$ region between 2800 and 3000cm^{-1}. The $\nu(C-C)$ region was normalized to the height of the peak at 1050cm^{-1} prior to peak fitting. Peak fitting of the $\delta(CH_{2/3})$ region was performed without prior normalization. The regions of the Raman spectra around 1300cm^{-1} and 1440-1458cm^{-1} along with the ratio of the integrated areas of the $\delta_a(CH_3)$ to $\delta(CH_2)$ peaks are given in Fig. S3. Note in Fig. S3C, the ratio $A(\delta_a(CH_3))/A\delta(CH_2)$ decreases monotonically with temperature down to the glass transition reflecting the slowing of local motions in the alkyl chains. The $\nu(CH_{2/3})$ region was normalized based on the integrated area between 2800 and 3000cm^{-1}.

Analysis of Dielectric Spectra

The dielectric spectra of the $[P_{666,14}]^+[BH_4]^-$ ionic liquid obtained at various temperatures was shown in Figure 3 in the main text. The frequency dependent dielectric data are well-described by a linear combination of empirical Havriliak-Negami (HN) functions with the random barrier model (RBM) to account for ion transport and a power law function of the radial frequency, ω, to account for electrode polarization effects in the low-frequency portion of the spectra, given by Equation S7.(11)

$$\varepsilon^*(\omega) = \sum_{i=1}^{n}\left[\frac{\Delta\varepsilon_i}{[1+(i\omega\tau_i)^{\beta_i}]^{\gamma_i}}\right] + \frac{\sigma_0}{\varepsilon_0}\left[\frac{\tau_e}{\ln(1+i\omega\tau_e)}\right] + A\omega^{-\lambda} + \varepsilon_\infty \quad [7]$$

The solid black lines in Figure 3 (main text) represent fits using Equation S7, where $\Delta\varepsilon_i$ is the dielectric relaxation strength, τ_i is the relaxation time, β_i is the symmetric stretching parameter, and γ_i is the asymmetric stretching parameter for the HN functions in the first term. The second term represents the RBM where σ_0 is the DC conductivity, τ_e is the characteristic ion diffusion time, and ε_0 is the vacuum permittivity. The third term accounts for the parasitic effects of electrode polarization which can obscure dipolar relaxations in the sub-α region of the dielectric spectra due to accumulation of ions at the electrode surface. A fractal power law is used to correct for the low-frequency electrode polarization contribution where A is the pre-exponential factor and λ describes the fractal nature of the phenomenon.(11–13) The final parameter, ε_∞ is the limiting high-frequency permittivity. The empirical HN function accounts for non-ideal dipolar relaxations with a distribution of relaxation times associated with reorientation of dipoles in the alternating electric field while the RBM accounts for charge transport in which charge carriers diffuse in a random, spatially heterogeneous potential energy landscape(11, 14–17). For charge transport to occur, the ions must hop over the randomly distributed energy barriers. The analytical expression of the RBM is obtained from the continuous-time-random-walk approximation assuming a non-interacting charge carrier isolated in a random energy landscape.(18–21) The RBM combined with the appropriate number of HN functions and the power law accounting for the low-frequency dispersion due to electrode polarization quantitatively describes the data as shown in Figure 3 (main text). The number of HN functions required to describe the data varied with the temperature of the sample. In general, the structural dynamics of the ionic liquid are described by an HN function denoted with the subscript α for the primary relaxation. The structural dynamics of the ionic liquid are coupled to the ion motion since this is a pure aprotic ionic material such that $\omega_\alpha \approx \omega_e$, where $\omega_i = 1/\tau_i$ is the relaxation rate (21). The coupling of the ion motion to the structural α relaxation indicates that ion hops are accompanied by local reorientation of surrounding ions(14). The $[P_{666,14}]^+[BH_4]^-$ ionic liquid also shows a secondary relaxation observed at high frequencies and low temperatures denoted as a beta process by the subscript β, which is has been associated with librations of the alkyl chains on the cation(17) and will not be discussed further. An additional HN function is necessary to fit the emergent slow, sub-α process that appears in the spectra of $[P_{666,14}]^+[BH_4]^-$ at and below 220K.

The derivative representation of the imaginary part of the complex dielectric function, defined as $\varepsilon''_{der} = (-\pi/2)\,[\partial\varepsilon'/\partial\ln(\omega)]$ based on the Kramers-Kronig relation(11), plotted versus radial frequency, ω, at various temperatures in Figure 3C in the main text reveals the relaxation behavior without the strong contribution from DC ionic conductivity. This representation allows for the observation of slow dynamics at frequencies below the characteristic ion diffusion rate. In this representation, the primary alpha relaxation is observed as a symmetric peak with a peak maximum at $\omega_\alpha \approx \omega_e$. It is clear that a slower, sub-α relaxation peak emerges at lower temperatures approaching the glass transition temperature for $[P_{666,14}]^+[BH_4]^-$. Observations of an emergent sub-α relaxation in super-cooled IL systems have not been previously reported in the literature suggesting a new type of behavior in ILs. This emergent sub-α process may be associated with the formation of polarizable interfaces between the ion-rich domain and the alkyl-rich domain on the nanoscale as the dynamics of the system slow down near the glass transition temperature. A slow dielectric relaxation in other IL systems has been previously reported and attributed to interfacial polarization occurring at the boundary between polar and nonpolar regions of the liquid.(22–25) The assignment of the sub-α relaxation to polarization of the interface separating ion-rich and alkyl-rich domains has been corroborated by scattering and simulation studies showing aggregation of anions and cation headgroups into a polar region excluding the alkyl chains into spatially distinct nonpolar domains.(25–39) However the slow dielectric relaxation is not always observed in nanostructured ILs due to variations in the morphology and connectivity of the polar domain with cation structure and alkyl

chain length.(24, 40) The emergence of this interfacial polarization for these systems may indicate a structural change in the local environment as the ion motion slows upon cooling.

The procedure used to fit the dielectric data was as follows. First, the σ_0 values were picked based on the plateau in σ' and subsequently fixed in fitting attempts. The data was then fit across the entire frequency window in the ε' representation using the real part of Equation S7 initialized with reasonable estimates of the parameters based on visual inspection. Once satisfactory fits were obtained, the fit lines were converted to the derivative representation and compared to the derivative spectra computed from the data itself. The fits were deemed accurate if they described well both the ε' and the ε''_{der} representations. The static dielectric permittivity was calculated from the fitting results using $\varepsilon_s = \Delta\varepsilon_{sub-\alpha} + \Delta\varepsilon_\alpha + \Delta\varepsilon_\beta + \frac{\sigma_0\tau_e}{\varepsilon_0} + \varepsilon_\infty$, and contains contributions from electronic, orientation, ionic, and interfacial polarization.(41)

Analysis of DSC data

The heat capacity data, C_p, shown in Figure 4C in the main text reveal an asymmetric, calorimetric peak in the $[P_{666,14}]^+[BH_4]^-$ IL sample. This asymmetric peaks in heat capacity indicates that this ionic liquid undergoes a thermodynamic transition above the glass transition temperature.

The calorimetric peaks observed for $[P_{666,14}]^+[BH_4]^-$ suggest a first-order liquid-liquid transition similar to those reported for other glass-forming systems.(42–45) Analysis of the configurational entropy, which can be calculated from the heat capacity, can shed light on the thermodynamic behavior of these systems approaching the glass transition temperature from the supercooled liquid state by invoking the theory of Adam and Gibbs (AG) based on cooperatively rearranging regions which establishes a link between the temperature dependence of the configurational entropy, S_c, and the dynamics of the structural relaxation.(46–49) In Figure 4D, the calculated configurational entropy, S_c, was plotted versus temperature. The temperature-dependent configurational entropy was calculated from the heat capacity data using the formula given in Equation S8.(47)

$$S_c(T) = \Delta S_{fus} - \int_T^{T_{fus}} C_p^{melt}(T') - C_p^{cryst}(T') d\log T' \quad [8]$$

In this equation, S_c is the configurational entropy, T_{fus} is the temperature of fusion, $\Delta S_{fus} = \Delta H_{fus}/T_{fus}$ is the entropy of fusion, and T' is the integration variable associated with the $C_p(T)$ data. Since these systems do not readily crystallize, the heat capacity of the crystal state, C_p^{cryst}, was approximated using the limiting low-temperature heat capacity of the glassy state. The contribution from the entropy of fusion was accounted for by assuming the validity of a Vogel-Fulcher-Tammann (VFT) Adam-Gibbs (AG) form of the temperature dependence of the configurational entropy given by Equation S9.(47)

$$S_c(T) = S_\infty \left(1 - \frac{T_K}{T}\right) \quad [9]$$

Here S_∞ is the limiting value of $S_c(T \to \infty)$ and T_K is the Kauzmann temperature where $S_c(T)$ becomes zero. The definition of the VFT-AG form of the temperature dependence of $S_c(T)$ imposes the constraint $T_K = T_0$, where T_0 is the Vogel temperature from the VFT form of the temperature dependence of the relaxation rates given by Equations S10 and S11.(11, 47, 50)

$$\omega(T) = \frac{1}{\tau(T)} = \omega_\infty \exp\left[\frac{-DT_0}{T - T_0}\right] \quad [10]$$

$$\log_{10}(\omega) = \log_{10}\omega_\infty + \frac{-DT_0 \log_{10} e}{T - T_0} \quad [11]$$

Here ω_∞, D, and T_0 are constant parameters with respect to temperature. The Vogel temperature, T_0, was obtained from fits of the DC conductivity, σ_0, as a function of inverse temperature using Equation S11 along with the fact that $\sigma_0 \propto \omega_\alpha$ to describe the temperature dependence of the DC conductivity shown in Figure 4A in the main text. Parameters obtained from the VFT fits are given in Table S1 along with parameters from the VFT-AG fits to the $S_c(T)$ data. After numerical integration of the heat capacity data, the Vogel temperatures along with Equation S9 were utilized to adjust the magnitude of the configurational entropies so that $T_K \approx T_0$.

Although the high temperature configurational entropy data are well-described by the VFT-AG equation, shown as a dotted line in the plot in Figure 4D in the main text, the data deviate from VFT-AG behavior near the glass transition temperature. The configurational entropy falls off to a limiting low temperature value at higher temperatures than predicted by the VFT-AG form of the temperature dependence. Since configurational entropy accounts for all but the vibrational contributions to the entropy of the melt, this indicates that this IL undergoes a structural rearrangement that eliminates some of the accessible microstates of the melt approaching T_g(49).

Error Analysis

Error bars displayed in the graphs were obtained from the standard deviations of the fitting parameters.

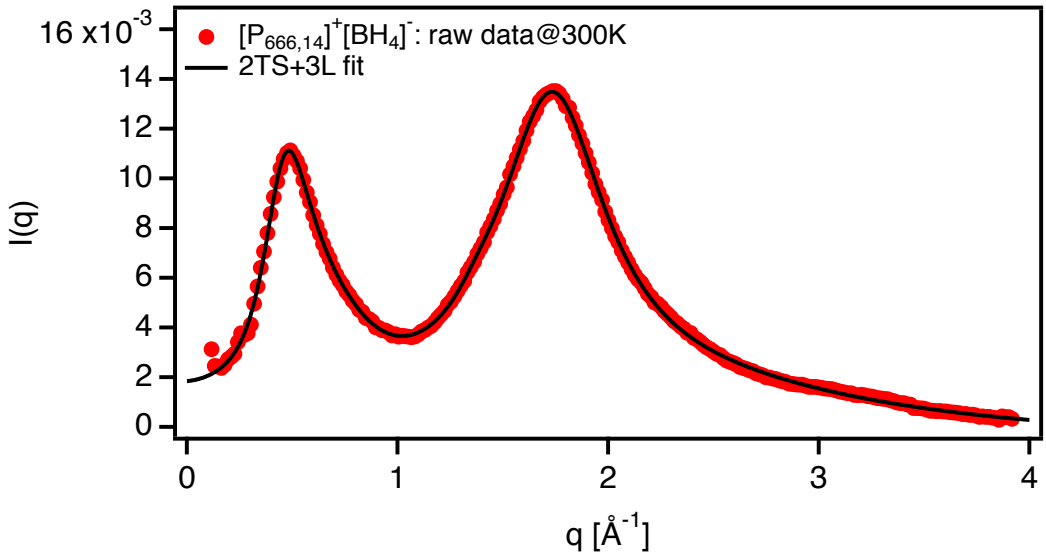

Fig. S1. Raw $I(q)$ data for $[P_{666,14}]^+[BH_4]^-$ at 300K.

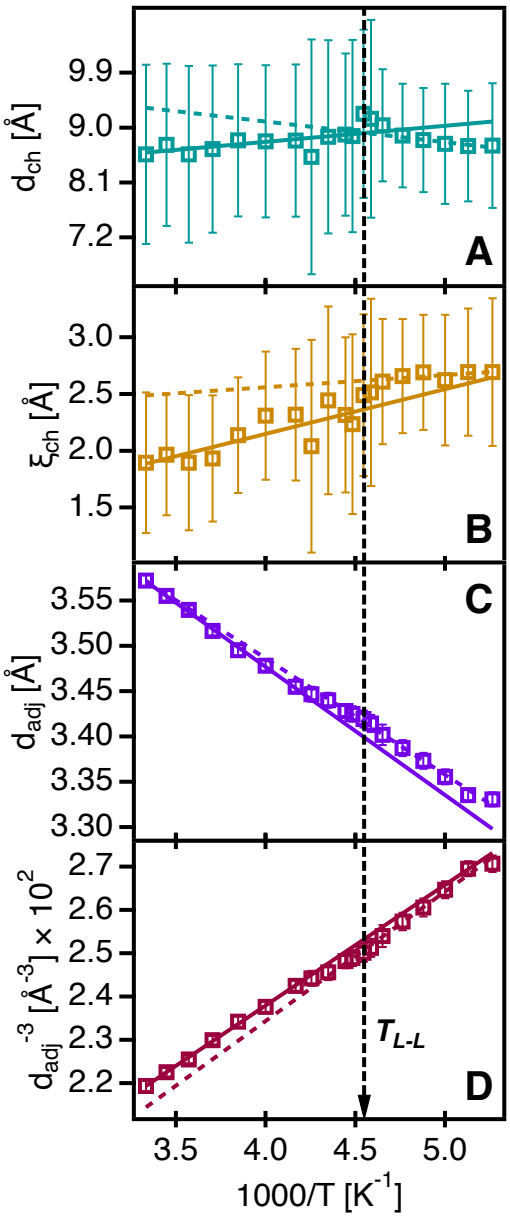

Fig. S2. Length scales of the charge alternation structure and the charge adjacency structure. **A** Charge alternation periodicity, d_{ch}, versus inverse temperature. **B** Charge alternation correlation length, ξ_{ch}. **C** Charge adjacency length, d_{adj}. **D** Inverse cube of d_{adj} serves as a proxy for density correlations. Solid and dotted lines represent fits to the data to serve a guides for the eye.

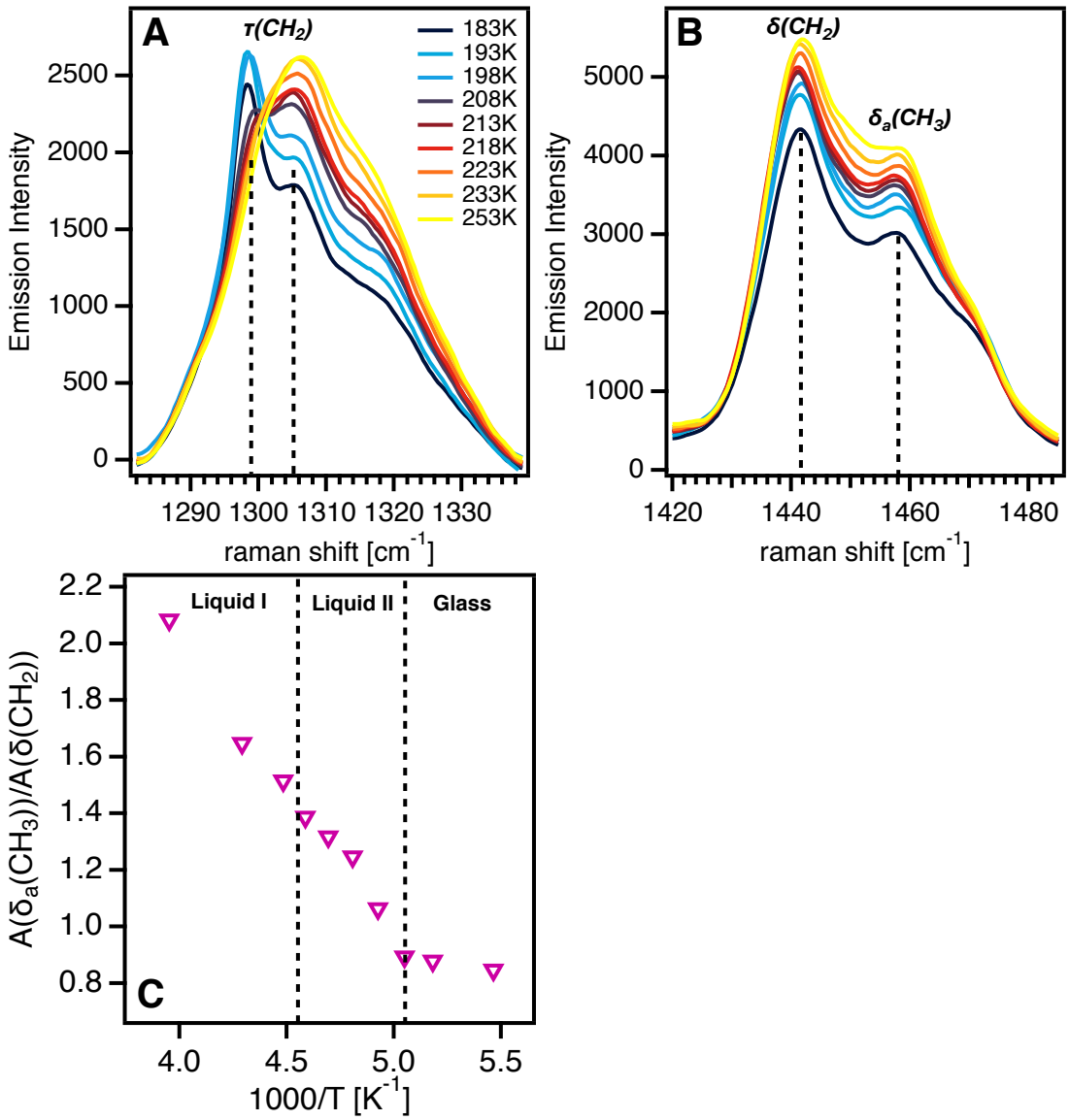

Fig. S3. Detail of Raman spectra. **A** Raman spectra of $[P_{666,14}]^+[BH_4]^-$ between 1280 and 1340cm^{-1} showing the $\tau(CH_2)$ modes. **B** Raman spectra of $[P_{666,14}]^+[BH_4]^-$ between 1420 and 1485cm^{-1} showing the $\delta(CH_2)$ modes. **C** Ratio of the integrated areas of the $\delta_a(CH_3)$ and $\delta(CH_2)$ modes.

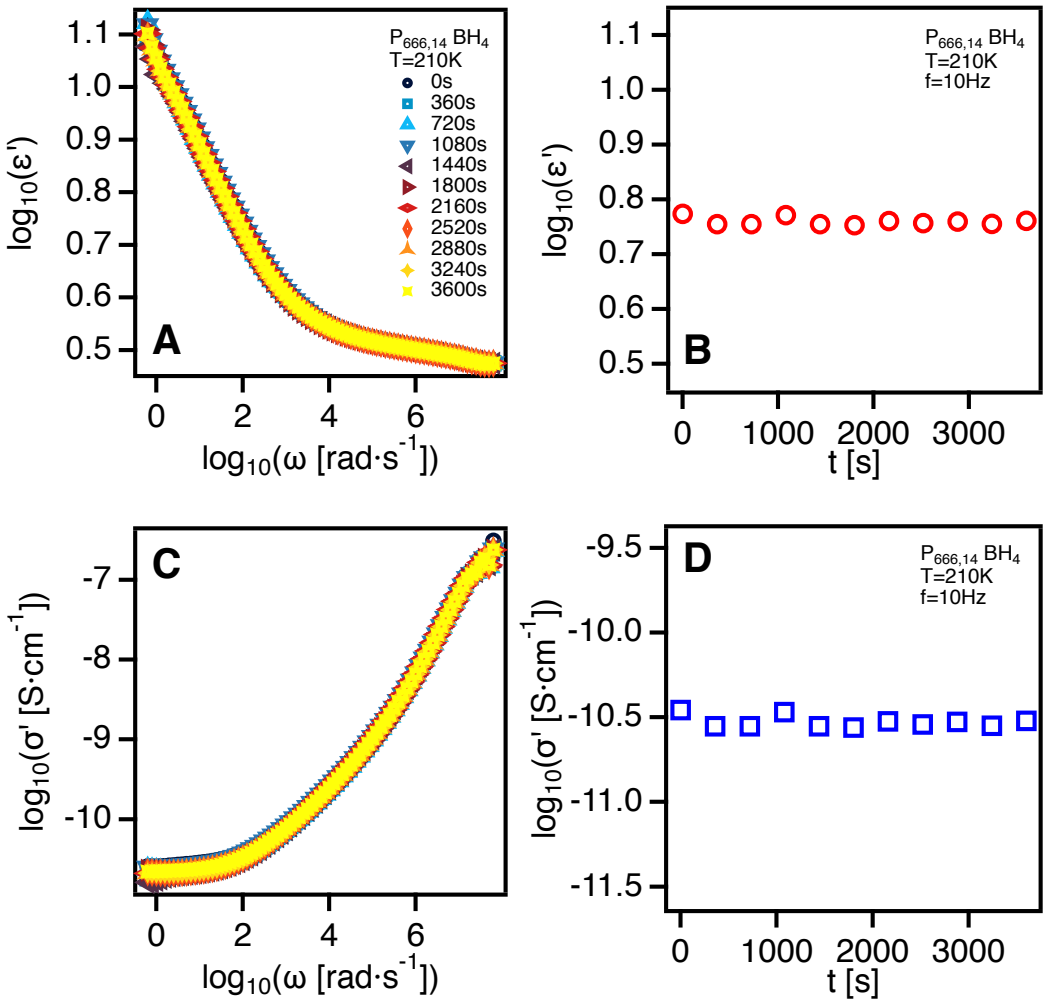

Fig. S4. Temporal evolution of dielectric spectra of $[P_{666,14}]^+[BH_4]^-$ at 210K measured over 1 hour. A Real part of the complex dielectric function, ε' versus radial frequency, ω. **B** Real part of the complex dielectric function, ε' versus time, t, at 10Hz. **C** Real part of the complex conductivity function, σ' versus radial frequency, ω. **D** Real part of the complex conductivity function, σ' versus time, t, at 10Hz.

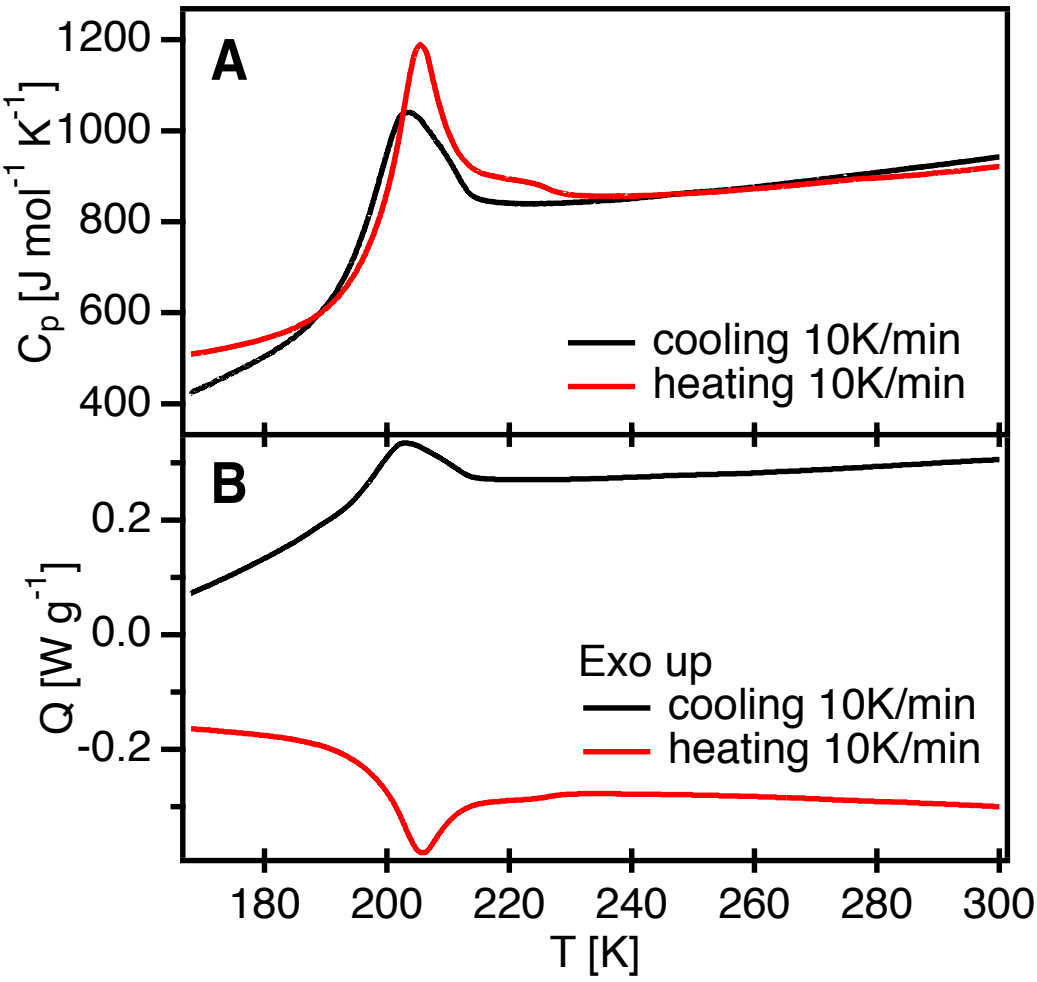

Fig. S5. Reversibility of DSC results. (**A**) Heat capacity of $[P_{666,14}]^+[BH_4]^-$ between 170K and 300K on cooling at 10K/min (black) and heating at 10K/min (red). (**B**) Heat flow of $[P_{666,14}]^+[BH_4]^-$ between 170K and 300K on cooling at 10K/min (black) and heating at 10K/min (red).

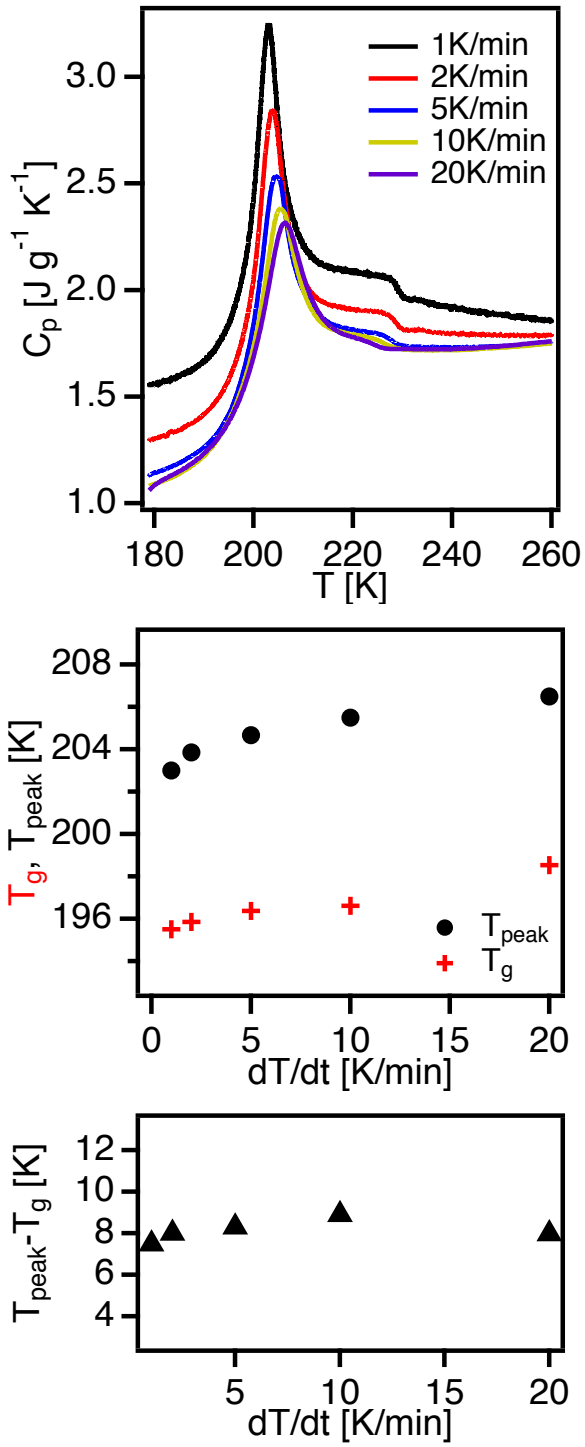

Fig. S6. Heating rate dependence of DSC results. A Heat capacity of $[P_{666,14}]^+[BH_4]^-$ between 180K and 260K at various heating rates. **B** Heating rate dependence of T_g and the temperature at the peak maximum, T_{peak}. **C** Heating rate dependence of the separation of T_{peak} and T_g.

Table S1. Parameters from VFT fits to $\sigma_0(T)$ and VFT-AG fits to $S_c(T)$ including glass transition temperatures, T_g, and fragilities, m.

	$\log \sigma_\infty$	D	T_0/K	$S_\infty/JK^{-1}mol^{-1}$	T_k/K	T_g/K	m
Liquid I	0.34±0.01	14.5±0.1	128.1±0.5	329.9±0.1	128.1±0.1	184.3	46.9
Liquid II	-4.0±1.0	2.9±1.1	176.8±6.4	661.0±1.5	173.4±0.1	198.0	100.0

References

1. CJ Bradaric, A Downard, C Kennedy, AJ Robertson, Y Zhou, Industrial preparation of phosphonium ionic liquids. *Green Chem.* **5**, 143–152 (2003).
2. KJ Fraser, DR MacFarlane, Phosphonium-based ionic liquids: An overview. *Aust. J. Chem.* **62**, 309–321 (2009).
3. N Bhawawet, JB Essner, DV Wagle, GA Baker, Ionic liquid anion controlled nanoscale gold morphology grown at a liquid interface. *Langmuir* **33**, 6029–6037 (2017) PMID: 28535055.
4. H Jin, et al., Physical properties of ionic liquids consisting of the 1-butyl-3-methylimidazolium cation with various anions and the bis(trifluoromethylsulfonyl)imide anion with various cations. *The J. Phys. Chem. B* **112**, 81–92 (2008) PMID: 18069817.
5. DV Wagle, AJ Rondinone, JD Woodward, GA Baker, Polyol Synthesis of Magnetite Nanocrystals in a Thermostable Ionic Liquid. *Cryst. Growth Des.* **17**, 1558–1567 (2017).
6. H Weiss, et al., Mesoscopic correlation functions in heterogeneous ionic liquids. *J. Phys. Chem. B* **121**, 620–629 (2017).
7. MI Ojovan, DV Louzguine-Luzgin, Revealing Structural Changes at Glass Transition via Radial Distribution Functions. *J. Phys. Chem. B* **124**, 3186–3194 (2020).
8. Y Marcus, Ionic and molar volumes of room temperature ionic liquids. *J. Mol. Liq.* **209**, 289–293 (2015).
9. H Tanaka, Bond orientational order in liquids: Towards a unified description of water-like anomalies, liquid-liquid transition, glass transition, and crystallization;Bond orientational order in liquids. *Eur. Phys. J. E* **35** (2012).
10. CJ Orendorff, MW Ducey, JE Pemberton, Quantitative correlation of Raman spectral indicators in determining conformational order in alkyl chains. *J. Phys. Chem. A* **106**, 6991–6998 (2002).
11. F Kremer, A Schönhals, eds., *Broadband Dielectric Spectroscopy.* (Springer, New York), (2003).
12. SH Liu, Fractal model for the ac response of a rough interface. *Phys. Rev. Lett.* **55**, 529–532 (1985).
13. HP Schwan, B Onaral, Linear and nonlinear properties of platinum electrode polarisation iii: Equivalence of frequency-and time-domain behaviour. *Med. Biol. Eng. Comput.* **23**, 28–32 (1985).
14. JR Sangoro, Charge transport and dipolar relaxations in an alkali metal oligoether carboxylate ionic liquid. *Colloid Polym. Sci.* **292**, 1933–1938 (2014).
15. JC Dyre, The random free-energy barrier model for ac conduction in disordered solids. *J. Appl. Phys.* **64**, 2456–2468 (1988).
16. JR Sangoro, et al., Diffusion in ionic liquids: The interplay between molecular structure and dynamics. *Soft Matter* **7**, 1678–1681 (2011).
17. T Cosby, Z Vicars, EU Mapesa, K Tsunashima, J Sangoro, Charge transport and dipolar relaxations in phosphonium-based ionic liquids. *J. Chem. Phys.* **147** (2017).
18. H Scher, M Lax, Stochastic transport in a disordered solid. i. theory. *Phys. Rev. B* **7**, 4491–4502 (1973).
19. TB Schrøder, JC Dyre, ac hopping conduction at extreme disorder takes place on the percolating cluster. *Phys. Rev. Lett.* **101**, 025901 (2008).
20. TB Schrøder, JC Dyre, Scaling and universality of ac conduction in disordered solids. *Phys. Rev. Lett.* **84**, 310–313 (2000).
21. JR Sangoro, F Kremer, Charge transport and glassy dynamics in ionic liquids. *Accounts Chem. Res.* **45**, 525–532 (2012) PMID: 22082024.
22. PJ Griffin, et al., Ion transport and structural dynamics in homologous ammonium and phosphonium-based room temperature ionic liquids. *J. Chem. Phys.* **142** (2015).
23. T Cosby, Z Vicars, Y Wang, J Sangoro, Dynamic-Mechanical and Dielectric Evidence of Long-Lived Mesoscale Organization in Ionic Liquids. *J. Phys. Chem. Lett.* **8**, 3544–3548 (2017).
24. T Cosby, Z Vicars, M Heres, K Tsunashima, J Sangoro, Dynamic and structural evidence of mesoscopic aggregation in phosphonium ionic liquids. *J. Chem. Phys.* **148** (2018).
25. T Cosby, U Kapoor, JK Shah, J Sangoro, Mesoscale organization and dynamics in binary ionic liquid mixtures. *The J. Phys. Chem. Lett.* **10**, 6274–6280 (2019) PMID: 31560210.
26. F Nemoto, et al., Neutron scattering studies on short- and long-range layer structures and related dynamics in imidazolium-based ionic liquids. *J. Chem. Phys.* **149** (2018).
27. R Hayes, GG Warr, R Atkin, Structure and Nanostructure in Ionic Liquids. *Chem. Rev.* **115**, 6357–6426 (2015).
28. A Triolo, et al., Thermodynamics, structure, and dynamics in room temperature ionic liquids: The case of 1-Butyl-3-methyl imidazolium hexafluorophosphate ([bmim][PF 6]). *J. Phys. Chem. B* **110**, 21357–21364 (2006).
29. A Triolo, O Russina, HJ Bleif, E Di Cola, Nanoscale segregation in room temperature ionic liquids. *J. Phys. Chem. B* **111**, 4641–4644 (2007).
30. RP Daly, JC Araque, CJ Margulis, Communication: Stiff and soft nano-environments and the "octopus Effect "are the crux of ionic liquid structural and dynamical heterogeneity. *J. Chem. Phys.* **147** (2017).
31. TL Greaves, et al., Fluorous protic ionic liquids exhibit discrete segregated nano-scale solvent domains and form new populations of nano-scale objects upon primary alcohol addition. *Phys. Chem. Chem. Phys.* **15**, 7592–7598 (2013).
32. F Lo Celso, A Triolo, L Gontrani, O Russina, Communication: Anion-specific response of mesoscopic organization in ionic liquids upon pressurization. *J. Chem. Phys.* **148**, 1–5 (2018).
33. JJ Hettige, JC Araque, CJ Margulis, Bicontinuity and multiple length scale ordering in triphilic hydrogen-bonding ionic liquids. *J. Phys. Chem. B* **118**, 12706–12716 (2014).
34. L Gontrani, et al., Liquid structure of trihexyltetradecylphosphonium chloride at ambient temperature: An x-ray scattering

and simulation study. *J. Phys. Chem. B* **113**, 9235–9240 (2009).
35. Y Ji, R Shi, Y Wang, G Saielli, Effect of the chain length on the structure of ionic liquids: From spatial heterogeneity to ionic liquid crystals. *J. Phys. Chem. B* **117**, 1104–1109 (2013).
36. JJ Hettige, HK Kashyap, CJ Margulis, Communication: Anomalous temperature dependence of the intermediate range order in phosphonium ionic liquids. *J. Chem. Phys.* **140**, 1–5 (2014).
37. T Pott, P Méléard, New insight into the nanostructure of ionic liquids: A small angle X-ray scattering (SAXS) study on liquid tri-alkyl-methyl-ammonium bis(trifluoromethanesulfonyl)amides and their mixtures. *Phys. Chem. Chem. Phys.* **11**, 5469–5475 (2009).
38. JJ Hettige, JC Araque, HK Kashyap, CJ Margulis, Communication: Nanoscale structure of tetradecyltrihexylphosphonium based ionic liquids. *J. Chem. Phys.* **144** (2016).
39. HK Kashyap, et al., Temperature-dependent structure of ionic liquids: X-ray scattering and simulations. *Faraday Discuss.* **154**, 133–143 (2012).
40. K Shimizu, MF Costa Gomes, AA Pádua, LP Rebelo, JN Canongia Lopes, Three commentaries on the nano-segregated structure of ionic liquids. *J. Mol. Struct. THEOCHEM* **946**, 70–76 (2010).
41. EI Izgorodina, M Forsyth, DR MacFarlane, On the components of the dielectric constants of ionic liquids: Ionic polarization? *Phys. Chem. Chem. Phys.* **11**, 2452–2458 (2009).
42. SSN Murthy, Liquid–liquid transition in polymers and glass-forming liquids. *J. Polym. Sci. Part B: Polym. Phys.* **31**, 475–480 (1993).
43. I Kaori, M CT, C Angell, Thermodynamic determination of fragility in liquids and a fragile-to-strong liquid transition in water. *Nature* **398** (1999).
44. KI Murata, H Tanaka, Liquid-liquid transition without macroscopic phase separation in a water-glycerol mixture. *Nat. Mater.* **11**, 436–443 (2012).
45. Z Wang, et al., Liquid-liquid phase transition and its phase diagram in deeply-cooled heavy water confined in a nanoporous silica matrix. *J. Phys. Chem. Lett.* **6**, 2009–2014 (2015).
46. G Adam, JH Gibbs, On the temperature dependence of cooperative relaxation properties in glass-forming liquids. *The J. Chem. Phys.* **43**, 139–146 (1965).
47. R Richert, CA Angell, Dynamics of glass-forming liquids. V. On the link between molecular dynamics and configurational entropy. *The J. Chem. Phys.* **108**, 9016–9026 (1998).
48. MD Ediger, P Harrowell, Perspective: Supercooled liquids and glasses. *J. Chem. Phys.* **137** (2012).
49. L Berthier, M Ozawa, C Scalliet, Configurational entropy of glass-forming liquids. *J. Chem. Phys.* **150** (2019).
50. C Iacob, et al., Charge transport and glassy dynamics in imidazole-based liquids. *J. Chem. Phys.* **129** (2008).